

NOTE TO USERS

Page(s) missing in number only; text follows. The manuscript was microfilmed as received.

122

This production is the best copy available.

UMI[®]

PREVIEW

MAGNETIZATION PRECESSION OF MAGNETIC THIN
FILMS STUDIED BY ALL OPTICAL PUMP-PROBE
TECHNIQUE.

by

Steven A. Michalski

A DISSERTATION

Presented to the Faculty of
The Graduate College at the University of Nebraska
In Partial Fulfillment of Requirements
For the Degree of Doctor of Philosophy

Major: Physics and Astronomy

Under the Supervision of Professor Roger D. Kirby

Lincoln, Nebraska

December 2007

UMI Number: 3294903

PREVIEW

UMI[®]

UMI Microform 3294903

Copyright 2008 by ProQuest Information and Learning Company.
All rights reserved. This microform edition is protected against
unauthorized copying under Title 17, United States Code.

ProQuest Information and Learning Company
300 North Zeeb Road
P.O. Box 1346
Ann Arbor, MI 48106-1346

MAGNETIZATION PRECESSION OF MAGNETIC THIN FILMS STUDIED BY ALL
OPTICAL PUMP-PROBE TECHNIQUE.

Steven A. Michalski, Ph.D.

University of Nebraska, 2007

Advisor: Roger D. Kirby

The study of magnetization dynamics such as magnetization precession and precessional damping provides insights into the behavior of complex magnetic systems, and indeed may lead to a better understanding of the fundamental limits of magnetic reversal process. In this work, a time-resolved magneto-optic Kerr effect system (TRMOKE) was developed to study magnetization dynamics: Precession and damping. The system uses a femtosecond laser in a pump-probe experiment with direct optical excitation, very similar to the method introduced by Ganping Ju and coworkers. Also, a model based on the Landau-Lifshitz-Gilbert equation (LLG) was developed and used to interpret and analyze the experimental magnetization precession data of a single magnetic layer. The model can be used to predict the precession frequencies with and without damping, the eigenvectors of the magnetization and allows the Gilbert damping parameter (α) to be determined. The model is extended to a system of two magnetic layers coupled through a nonmagnetic spacer layer. The capabilities of the TRMOKE system and the LLG models, were demonstrated by studying the magnetization dynamics of Ni/Pt bilayers.

Static and dynamic magnetic properties of exchange-coupled magnetic layers have been investigated by magneto-optical measurements. The samples are [Pt/Co] multilayers with perpendicular magnetic anisotropy (PMA) exchange-coupled to a Co layer with in-plane magnetic anisotropy. The exchange is indirect, realized and tuned by an intervening Pt layer of varying thickness. Both the strength and the angle of an external applied magnetic field were varied and for many samples, two modes with two distinct precession frequencies were observed in the precession measurements. The frequencies of both modes depend on the strength and the angle of the applied magnetic field. The LLG model predicts two precessional modes (“acoustic” and “optic”) whose behaviors depend on the strength and sign of the exchange coupling. The model is in good qualitative agreement with the data and allows us to estimate the magnitude of the exchange coupling between the two layers.

Acknowledgements

I would like to acknowledge my appreciation to all those that supported, helped, advised, funded, taught, accepted, inspired or keep me sane by being a friend, including but not exclusive to:

Dr. Roger Kirby	Dr. Mike Bonder	Brian Jones
Dr. David Sellmyer	Dr. Robyn Wilde	Dr. Bob Kelty
Dr. Sitaram Jaswal	Dr. Richard Thomas	Brian and Beth Farleigh
Dr. John Woollam	Dr. Mark Meldrim	Shelli Krupicka
Dr. Ralph Skomski	Dr. Carl Lundstedt	Verona Skomski
Dr. Jian Zhou	Scott Wadewitz	Theresa Sis
Dr. Nikolay Polushkin	Bob Buckley	Kay Haley
Dr. Christian Binek	Bob Mumgaard	Jenny Becic
Dr. Minglan Yan	Zhen Li	Patty Christen and company
Dr. Sy-Hwang Liu	Tom George	Mike Jensen and company
Dr. Mingjun Yu	Annie George	Les Marquart
Dr. Hao Zheng	Shawn Langan	The NSF-MRSEC
Dr. Aliekber Aktag	James Glasbrenner	The W.M. Keck Foundation
Dr. Yucheng Sui	Dr. Adam Green	Nebraska Center for
Dr. Jun Zhang	Mikhail Bragin	Materials and Nanoscience
Dr. Korey Sorge	Christopher Barten	Department of Physics and
Dr. Maria Daniil	Andrew Baruth	Astronomy

Table of Contents

Chapter 1: Introduction	1
Chapter 2: Experimental Procedures	7
2.1 Sample Deposition	7
2.2 Structural Characterization	9
2.3 Magnetic Characterization	10
2.4 MOKE	11
Chapter 3: Theory of Ultrafast Magnetization Dynamics	13
3.1 Three temperature model	14
3.2 Precessional Dynamics of a Single Magnetic Layer	19
3.2a Landau-Lifshitz-Gilbert equation	20
3.2b The effective field terms	21
3.2c The equilibrium position of the magnetization	25
3.2d Magnetization dynamics	27
3.2 Precessional Dynamics of Indirect Exchange Coupled Magnetic Layers	30
3.3a RKKY coupling	31
3.3b Magnetization dynamics of two coupled magnetic layers	32
Chapter 4: Magnetization Precession Measurements.	41
4.1 All optical pump-probe system.	44
4.2 An example: Ni/Pt bilayer.	52

4.3 Conclusion	64
Chapter 5: Coupled Precession Modes in Indirect Exchange-Coupled [Pt/Co]-Co Thin Films	65
5.1 Experimental	66
5.1a Sample preparation and characterization	66
5.1b Pump-probe technique	72
5.2c Data analysis	73
5.2 Results and Discussion	75
5.2a The individual Co layer and Pt/Co Structure	75
5.2b The exchanged-coupled samples: [Pt / Co] ₄ / x Å Pt/ Co	75
5.3 Conclusions	86
Chapter 6: Summary and Conclusions	87
References	92
Appendix A: The Mira and Cavity dumper.	108
A.1: The Mira System	108
A.2: The Cavity Dumper	112
A.3: Daily Operation	115
A.4: Usage Tips	120
Appendix B: FORTRAN Programs	123
1. Resonance.for	124
2. EnergytwodampT1.for	131
Appendix C: LabVIEW Programs	146
1 StageControl.vi	147

2	AutoKerrDelay.vi	159
3	HLoopforMira.vi	174
Appendix D: List of Publications		186

PREVIEW

List of Figures

Figure 2.1 Sputtering rate as a function of the power of the sputtering gun for various target	9
Figure 3.1 The effects of laser heating of a magnetic film.	15
Figure 3.2 The numerical solutions to equations 4.1-4.3 for a nickel film.	17
Figure 3.3 The torque τ_{Ani} on the magnetization due to the uniaxial anisotropy.	24
Figure 3.4 Geometry used in calculating the equilibrium position of the Magnetization	26
Figure 3.5 Calculated frequency curves without damping (solid lines) and with damping (dashed lines)	29
Figure 3.6 Calculated frequency curves without damping (solid lines) and with damping (dashed lines)	29
Figure 3.7 The geometry used to calculate the precession dynamics of two magnetic layers M_1 and M_2 separated by a spacer layer	34
Figure 3.8 Schematic pictures of both precession modes	35
Figure 3.9 The calculated precession frequencies as a function of H applied at 45 degrees for various values of ferromagnetic coupling.	37
Figure 3.10 The calculated precession frequencies as a function of applied field angle with H = 6 kOe for various values of ferromagnetic coupling.	37
Figure 3.11 The calculated precession frequencies as a function of H applied at 45 degrees for various values of antiferromagnetic coupling	39

Figure 3.12 The calculated precession frequencies as a function of applied field angle with $H = 6$ kOe for various values of antiferromagnetic coupling.	39
Figure 4.1 Schematic of a strip line geometry photoconductive circuit	43
Figure 4.2 Schematic of all optical pump-probe precession measurement system.	44
Figure 4.3 A simplified schematic of the system with the electronics shown but without the optical components.	48
Figure 4.4 A picture and a schematic of the permanent magnetic holder used to rotate the magnetic field in the YZ plane	50
Figure 4.5 X-ray reflectivity measurements for the [5 nmPt/5 nmNi] sample and the fit used to calculate the thickness.	54
Figure 4.6 AGFM in plane hysteresis loops for samples: [10 nm Pt/7.5 nm Ni], [10 nm Pt/5 nm Ni], [5 nm Pt/10 nm Ni] and [5 nm Pt/5 nm Ni] normalized to the volume of each sample.	54
Figure 4.7 a) a typical time delay scan on the 5nm Pt/7.5nm Ni sample. b) A discrete Fourier Transform of the data in a) to determine the precession frequency.	56
Figure 4.8 Δ Kerr signal as a function of pump-pulse delay for Ni = 3nm, 5nm, 7.5nm and 10nm with a Pt layer of 5nm. The pump fluence = 13.6 mJ/cm^2 and the applied field was 5.1kOe applied at 45 degrees. Note the different time axis scale for the 3nm Ni film.	60
Figure 4.9 Shows delay scan of the 5nm Pt/5nm Ni film taken with different pump pulse fluences (F) = 13.6, 8.5, and 2.1 mJ/cm^2 .	60

Figure 4.10 The calculated Gilbert damping parameter α for the different Ni layer thicknesses and different fluences. The solid line represents the average α for each of the Ni layers 62

Table 4.1 Summary of α 's and the frequencies extracted from the fitting technique for each Ni thickness for the different fluences. 63

Figure 5.1. A schematic of the sample structure and the orientation of the magnetizations in the Co and Pt-Co layers with a) no coupling between the layers and b) ferromagnetic coupling between the layers. 67

Figure 5.2. X-ray diffraction from samples; 50 Å Co /20 Å Pt, and 20 Å Pt/[Pt 5 Å / Co 4 Å]₄/20 Å Pt and 15 Å Pt/[Pt 5 Å / Co 4 Å]₄/15 Å Pt/50 Å Co/20 Å Pt. 67

Figure 5.3 Polar MOKE hysteresis loops for the two base samples and for various Pt spacer layer thicknesses. 69

Figure 5.4 AGFM Hysteresis measured for the two base samples. a) in-plane Co loops and b) out-of-plane Pt/Co loops. 70

Figure 5.5 Partially SQUID out of plane and in-plane hysteresis half loops of the sample Si/ 2 nm Pt/[Pt 5 Å / Co 4 Å]₄/2 nm Pt. The line is the low field extrapolation used to estimate K_1 . 72

Figure 5.6 A simulation of the transform of equation 5.3 for the two modes being in phase and completely out of phase. 74

Figure 5.7 a) a typical time delay scan on the 5nm Co/2 nm Pt sample red points and the fit solid black line used to determine the Gilbert damping constant and the precession frequency. b) A discrete Fourier Transform of the data in a) to determine the precession frequency. 76

Figure 5.8 a) A typical time delay scan on the Si/ 2 nm Pt/[Pt 5 Å / Co 4 Å]₄/2 nm Pt

b) A discrete Fourier transform of the data in a) to determine the precession

frequency. 76

Figure 5.9(a) The precession frequency as function of applied strength with $\theta_H = 45^\circ$ for

both the Co layer and the Pt/Co multilayers. (b) The precession frequencies

vs applied field angle ($H = 4.6$ kOe). 77

Figure 5.10 (a) Typical pump-probe signals as a function of time for the sample with

$x=15$ Å Pt spacer layer for various angles with respect to the sample normal of

a 4.5 kOe applied field. (b) The Fourier transforms of the data in (a) (points)

and our least squares fits of the transform (lines). 79

Figure 5.11 (a) Typical pump-probe signals as a function of time for the sample with $x =$

21 Å Pt spacer layer for various angles with respect to the sample normal of a 8.2

kOe applied field. (b) The Fourier transforms of the data in (a) (points) and our

least squares fits of the transform (lines). 79

Figure 5.12 Δ Kerr vs time delay scan and DFT for $x = 18$ Å Pt spacer layer a) and b), $x =$

25 Å c) and d), and $x = 30$ Å e) and f) for various angles of the applied field. The

solid lines in the DFT graphs are the least squares fits of the transform. 80

Figure 5.13 (a) shows the delay curve for the 9 Å Pt spacer layer at various angles of a

4.6 kOe applied field, and (b) the DFT of the data in (a). The lines are a guides

for the eye. 81

Figure 5.14 Δ Kerr vs time delay scan and DFT for $x = 3$ Å Pt spacer layer a) and b), $x = 6$

Å c) and d), and $x = 12$ Å e) and f) for various angles of the applied field. The

solid lines in the DFT graphs are a guide to the eye. 82

Figure 5.15 The mode frequency as function of applied field angle for the samples with Pt spacers layers = 15 Å (red circles) and 25Å (blue squares) and the LLG predicted mode frequencies for coupling constant $J = 0.3 \text{ erg/cm}^2$ (solid black lines) and $J = 0.001 \text{ erg/cm}^2$ (solid magenta lines). The magnitude of the applied field was 4.5 kOe. 84

Figure 5.16 the field dependence of the frequency for the $x = 2.1 \text{ nm}$ sample. The field angle was 70 degrees. The circles are the data and the black lines are the predicted frequencies 85

Figure A.1 Optical Schematic of Mira in normal operation taken for reference 1 109

Figure A.2 intensity of the light in the cavity for a different number of mode with random phases and in phase (from Ref. 1). L is the cavity length and c is the speed of light. 110

Figure A.3 Optical schematic of the Mira and cavity dumper used together. The red lines are the main laser beam in the cavity and the blue lines the diffracted beam BP Brewster prism. Note, CM3 is the output coupler labeled M1 in figure A. 113

Figure A.4 A block diagram of the Mira and cavity dumper with controllers and electronics. 114

Figure A.5 The top of the cavity dumper. 115

Figure A.6 The top of the part of the Mira where the pump laser enters the Mira. 115

Figure A.7 The oscilloscope image of the output of the fast photodiode of the Mira showing the pulse train and the diffraction efficiency. 118

Figure A.8 Display of Ocean Optic Spectrometer program. 120

Chapter 1: Introduction

In today's technological world magnetic devices are used in televisions, computers, cars and almost every electrical device. In the future, magnetic materials and magnetic devices will continue to play an important part in technology from computer hard drives to new spintronic sensors and actuators. Improvements in technology require an improvement in the magnetic materials used in magnetic and electronic devices. A perfect example is the improved performance of magnetic hard drives. Due to the increasing demand to store and manipulate large amounts of data, the magnetic recording industry has dramatically increased the capacity and performance of magnetic hard drives. The hard drive capacity has increased due to new and novel magnetic materials¹⁻⁸, the introduction of new techniques such as perpendicular magnetic recording⁸⁻¹⁴, and the discovery and application of Giant Magneto Resistance^{15,16} (GMR). A GMR element (read head) consists of two ferromagnetic layers separated by a nonmagnetic layer. The electrical resistance of the element depends on the relative orientation of the magnetizations in the ferromagnetic layers. Since the orientation of the magnetization can be changed by an external magnetic field, for example as created by a closely placed magnetic domain wall, the GMR read head is a very sensitive magnetic field sensor. The increased sensitivity not only improved the read performance of the magnetic read head but allowed for an increase in the storage capacity of the hard drive by reducing the bit size required to obtain a good signal to noise ratio. This continued increase in performance of magnetic materials will lead to improvements in existing technology and will give rise to new technologies in the future.

The emerging field of spintronics has led to the development of new magnetic devices such as spin valves¹⁶⁻²⁵ which include GMR elements, magnetic random access memory (MRAM)²⁵⁻²⁹, spin transistors³⁰⁻³⁴, and spintronic biosensors³⁵⁻³⁷. Spintronics devices exploit the spin of the electrons not just the electrical charge. Spintronics devices work by encoding data into the spin of electrons. For example, spin-polarized electrons can be sent down a wire as current, and another spintronic device can read the spin information transmitted. This adds an extra degree of freedom in designing and producing new technologies.

As the amount of data continues to increase, hard drives and spintronic devices will need to be able to operate at fast speeds, which in turn requires a faster way to control the magnetization in the magnetic materials in those devices. This control can be complete reversal of the magnetization for magnetic hard drives or simply reorientation of the magnetization into a new stable state. For magnetic recording, the speed of writing magnetic data depends on the switching characteristic of the magnetic material used and the method used to produce a reversal of the magnetization. In last two decades, much research focused on developing techniques to increase the speed of complete magnetic reversal. Much of this research has focused on increasing the speed of reversal by using magnetic pulses. At first, magnetic pulses were produced by a coil or strip line circuit that was mechanically or lithographically produced and powered by a bank of capacitors. These systems could produce large pulsed field in a small area but were limited to pulse widths of about a nanosecond³⁸⁻⁴⁰.

Recent advances in ultrafast pulsed lasers have lead to the development of pump-probe techniques to produce and utilize fast magnetic pulses in the study of

magnetization dynamics. In pump-probe experiments, the ultrafast laser pulse is split into two parts: Pump pulse and a probe pulse, with the pump pulse being used to perturb the system and the probe pulse to measure the subsequent properties of the system. Such experiments have provided unprecedented time resolution in the study of magnetization and electronic dynamics, and they are discussed in more detail in Chapter 4. A common technique developed by Freeman and others to generate picosecond magnetic pulses is to use a photoconductive circuit⁴¹⁻⁴⁶. The circuits are usually strip line or coil geometries of copper or gold lithographically patterned onto semiconducting GaAs substrates. The pump pulse strikes the GaAs, temporarily making it a conductor and thus launches a current pulse which generates a magnetic field pulse. The probe pulse arrives later and measures the change in the magnetization induced by the magnetic field pulse using Faraday or Kerr magneto-optical effect. The magnetic fields produced by these methods can have pulse widths down to picoseconds if high quality low-temperature grown GaAs is used⁴⁷.

The development of fast magnetic pulses and the need to increase the write speed of hard drives and MRAM has lead to renewed interest in precessionally assisted magnetic switching⁴⁸⁻⁵². In conventional magnetic reversal, a sufficiently large static magnetic field is applied in the opposite direction to the magnetization. This increases the internal energy of the system making it favorable for the magnetization to reverse. In precessional switching, a magnetic field pulse is applied which changes the equilibrium orientation of the magnetization which then can precess into the reversed direction. This process depends on the intrinsic precessional dynamics of the system. The advantage of this technique is the field pulses are fast and thus switching times can be fast. The

maximum reversal rate using this method would be one half of the precessional frequency, typically in the 10-100 GHz range⁵³⁻⁵⁵. One problem with this technique is the ringing of the magnetization. During the precession, the magnetization tends to oscillate between states (ringing) until the precession is stopped by damping or some other mechanism. Recently, precessional magnetic switching in soft magnetic materials such as permalloy has been observed^{49,56-59} and control of the precession ringing has been demonstrated using another magnetic pulse to stop the precession^{43,46,59,60}.

It would be ideal to control the magnetization without a magnetic field. Recent research has opened up the possibility of controlling the magnetization using electric fields or direct optical pulses. Electric field control of the magnetization relies on using materials that exhibit the magnetoelectric effect such as multiferroics, which are materials that have both ferromagnetic and ferroelectric properties^{61,62}. The magnetoelectric (ME) effect allows for the coupling of magnetic properties to an external electric field and couples the electrical properties to a magnetic field. Using the magnetoelectric effect, a magnetic bit could be written with an electric field instead of a magnetic field which could lead to faster memory. Partial control of the magnetization by an electric field has been observed in a composite thin film of Co/Pd – Pb(Zr_xTi_{1-x})O₃ by Kim *et al.*⁶³. Magnetic control of the electric polarization has been demonstrated⁶⁴ and also electric field control of the exchange bias field has been reported⁶⁵ using ME materials.

Optical control of the magnetization also has very promising potential. Recent experiments show the optical pulses can give a rise to a rapid demagnetization of magnetic thin films⁶⁶⁻⁷⁵, a reduction in magnetic anisotropy⁷⁶ and changes in the exchange coupling strength and exchange bias field of magnetic multilayers⁷⁷⁻⁷⁹ on time

scales of a few picoseconds. All of these reports relied on the ultrafast heating of the electron, lattice, and spin systems of the magnetic material produced by a direct optical excitation to change the magnetic properties. The changes were not enough to induce a coherent reversal of the magnetization but such studies give insights into the magnetization dynamics. Another method of optical control has been proposed recently which relies on the inverse Faraday Effect⁸⁰⁻⁸⁵. The inverse Faraday effect produces an effective magnetic field pulse when an intense pulse of circularly polarized light passes through a magnetic material. The magnetic field strength is proportional to the intensity of the light pulse and Verdet constant of the sample⁸⁶. This technique opens the possibility of controlling the magnetization on time scales equal to the pulse width of the optical pulse. Complete magnetization reversal of $\text{Gd}_{22}\text{Fe}_{74.6}\text{Co}_{3.4}$ has been observed using circular polarized 40 fs pulses by Stanciu *et al.* in reference 85.

All the methods presented here deal with increasing the speed of the magnetization reversal. The work presented in this dissertation focuses on studying the magnetization dynamics of thin film magnetic systems. Precession frequencies and damping are measured in order to get a better understanding of the fundamental limits of magnetic reversal process. Primarily the work here focuses on studying magnetization dynamics of magnetic layers separated by a nonmagnetic material. The intervening nonmagnetic layer provides indirect exchange-coupling between the two magnetic layers. Such materials are scientifically interesting and important in various areas of nanotechnology. Similar systems are already used in spin valve devices¹⁶ such as field sensors, and such materials could be candidates for magnetic media for use in magnetic recording. The focus here is on spin-reorientation caused by competing magnetic

anisotropies, realized by exchange-coupling a Pt/Co multilayer structure with perpendicular magnetic anisotropy to a Co layer having the easy axis of the magnetization in the film plane. The interlayer exchange J is tuned by the varying the thickness of an intervening Pt spacer layer. This permits the control of magnetic properties by tuning exchange strength and perpendicular magnetic anisotropy, a feature of great practical importance.

In this study, we using an all optical pump-probe technique very similar to the method introduced by Ganping Ju *et al.*⁷⁷ who investigated the $\text{Ni}_{81}\text{Fe}_{19}/\text{NiO}$ exchange-biased system. Our system uses direct optical excitation, which changes the magnetic properties both electronically and thermally. Chapter 2 will give a brief introduction into the experimental techniques use to fabricate and study the samples. Chapter 3 gives a detailed description of the Landau-Lifshitz-Gilbert based theoretical models used to guide the experiments and interpret the data. Chapter 4 presents the pump-probe optical and electronic setup in great detail and gives an example of how the system works by studying Ni/Pt bilayers. Chapter 5 presents the study of the magnetization dynamics of indirect exchanged-coupled [Pt/Co]-Co thin films. Chapter 6 will summarize the results presented here and give some ideas for future study.

Chapter 2: Experimental Procedures

The thin film samples studied in this work were prepared by magnetron sputtering. The micro-structures of the samples were measured by X-Ray Diffraction (XRD) and are consistent with Transmission Electron Microscopy (TEM) measurements. The magnetic properties were measured by an Alternating Gradient Force Magnetometer (AGFM) and a Magneto-Optical Kerr Effect (MOKE) system. This chapter will describe the basic operations and procedures for each of these systems while leaving any necessary details to the following chapters as needed. The magnetization dynamics were measured by an all optical pump-probe Time Resolved Magneto-Optical Kerr Effect (TRMOKE) system which is presented in detail in Chapter 4.

2.1 Sample Deposition

The samples were fabricated in one of two homemade magnetron sputtering systems. The first system was based on equipment obtained from the Dale Corporation (Dale), which includes two DC sputtering guns and one RF gun contained in a large vacuum bell jar. A water cooled diffusion pump (Varian 6") backed by a mechanical pump is used to produce a base pressure of $2-3 \times 10^{-7}$ Torr. The other system is based on equipment received from the 3M Corporation (3M) and also contains two DC and one RF guns. The vacuum in the 3M system is achieved by a cryo-pump backed by a mechanical pump which gives base pressures normally in the $2-4 \times 10^{-7}$ Torr range.

In both systems, sputtering was done in a 5 mTorr argon environment. Substrates were mounted on a water cooled table which can hold 12 samples per sputtering run. The rotational position of the sample table is controlled by a stepper motor connected to a PC. The chamber is pumped down for roughly 14 hours or until the desired base pressure is reached. Multilayered films are produced by moving the substrates to positions above each target gun to sputter the specific amount of material needed. A QuickBasic program controls the time the substrate stays above each target based upon the calibrated sputtering rates. The targets (Co, Pt, and Ni) used for these study were normally purchased from the Kurt J. Lesker company with a 99.95% purity.

The sputtering rates are calibrated by cutting aluminum foil into approximately 1 inch squares. The foils are cleaned in alcohol by an ultrasound for 10 minutes. The foils are then weighed at least twice using a microbalance with a sensitivity of 0.1 μ g. The foils are mounted to the substrate table and the chamber is pumped down to the base pressure. Then the target materials are sputtered onto 3-5 foils at different sputtering powers and different exposure times. The foils are weighed again and the difference in mass is due to the sputtered material. The sputtering rate R at a given sputtering power is given by

$$R = \frac{T}{\Delta t} = \frac{\Delta m}{\rho A \Delta t} \quad (2.1)$$

for each target material. In equation 2.1 Δt is the sputtering time, Δm is the change of mass of the Al foil, A is the film area, T is the thickness of the sputtered material, and ρ is the density of the sputtered material, usually taken to be bulk value. Figure 2.1 shows the sputtering rate as a function of sputtering power for Pt, Co, and Ni targets, the lines

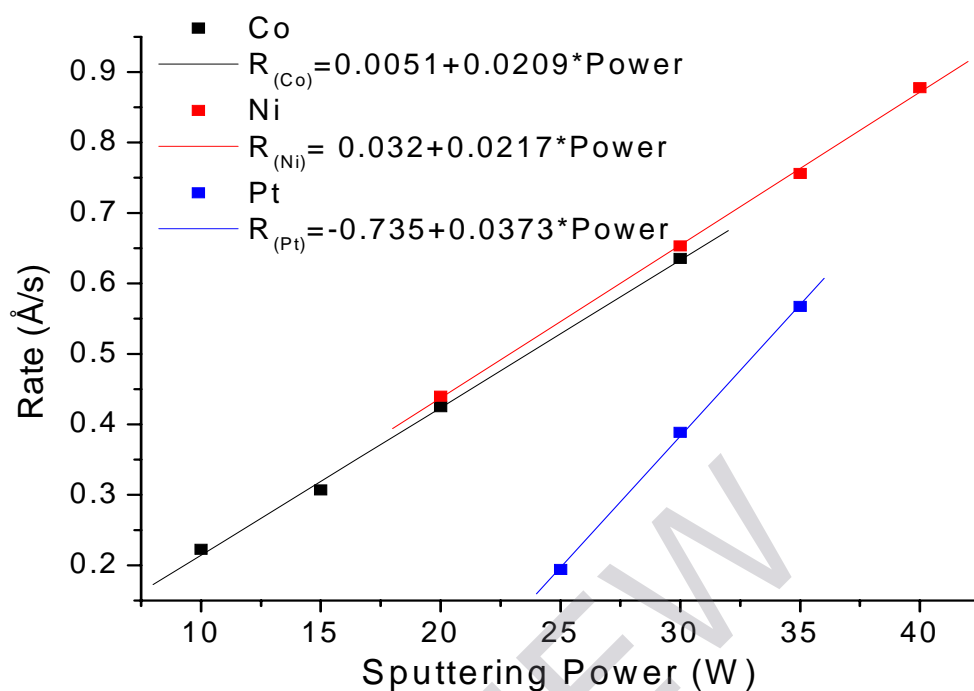


Figure 2.1 Sputtering rate as a function of the power of the sputtering gun for various targets.

represent the best linear fit to the data and the lines are used to calculate the rate at a given power.

2.2 Structural Characterization

The magnetic properties of the samples are dependent on the nanostructure of the sample; so, we need to understand the structure of the sample as much as possible. The nanostructures were measured by X-ray diffraction and transmission electron microscopy. X-ray diffraction was performed using a Rigaku DMAXB and a Bruker D8Discover